Advanced Materials

ADVANCED MATERIALS
www.advmat.de

RESEARCH ARTICLE

Engineering Heteroatomic Nanotraps in Vinyl-Benzazole COFs: Record Capacity and 99% Selectivity for Photocatalytic Gold Recovery From E-Waste

Quanquan Yang[1,2] | Shengxu Li[1] | Junyi Han[1] | Mengwei Chen[1] | Wenkai Zhao[1] | Sheng Wang[2] | Raul D. Rodriguez[3] | Tao Zhang[1]

[1]State Key Laboratory of Advanced Marine Materials, Ningbo Institute of Materials Technology and Engineering, Chinese Academy of Sciences, Ningbo, China | [2]School of Materials Science and Engineering, Zhejiang Sci-Tech University, Hangzhou, China | [3]Research School of Chemistry and Applied Biomedical Sciences, Tomsk Polytechnic University, Tomsk, Russia

Correspondence: Sheng Wang (wangsheng@zstu.edu.cn) | Raul D. Rodriguez (rodriguez@tpu.ru) | Tao Zhang (tzhang@nimte.ac.cn)

Received: 26 November 2025 | **Revised:** 8 January 2026 | **Accepted:** 13 January 2026

Keywords: covalent organic frameworks | electronic waste | gold recovery | heteroatomic nanotraps | photocatalytic

ABSTRACT

The recovery of gold from electronic waste is a critical environmental and technological challenge for a circular and sustainable economy. Conventional methods for gold recovery often suffer from low efficiency, poor selectivity, and reliance on harsh chemicals. In this work, we engineered three vinyl-azole-bridged covalent organic frameworks (COFs), systematically controlling heteroatom motifs to elucidate the structure-activity relationships behind gold ion adsorption and photocatalytic reduction. This strategic incorporation of azole-based units yielded hydrogen-bonded nanotraps along the pore walls, thereby maximizing active-site density and enhancing electrostatic interactions for the selective capture of gold ions. We found that all these COFs show gold adsorption capacities exceeding 3600 mg g^{-1}, with the thiazole-containing COF—featuring both nitrogen and sulfur—exhibiting the highest binding affinity and photocatalytic efficiency to a record value of 4658.1 mg g^{-1} under optimal conditions and a 99.2% efficiency for gold extraction. These results are confirmed by density functional theory (DFT) calculations, x-ray photoelectron spectroscopy, and real e-waste recovery experiments. The highly conjugated framework facilitates synergistic photoreduction of Au(III) to Au(0), exploiting the unique interplay between heteroatom chemistry, microenvironment engineering, and light-driven redox processes. This work introduces a new class of COF photocatalysts engineered with heteroatomic nanotraps, achieving exceptional gold recovery efficiency.

1 | Introduction

The ever-increasing global consumption of electronic devices goes hand in hand with the generation of electronic waste (e-waste), jeopardizing an environmentally safe future and sustainable resource management [1–4]. This problem is becoming even more critical as the significant computational demands of artificial intelligence could generate up to 82 million tons of e-waste by 2030 [5–7]. In this context, gold is a crucial material in resource recovery from e-waste due to its high economic value, strong chemical stability, and wide range of applications in electronics [8], energy storage [9], and catalysis [10, 11]. The conventional technologies for gold recovery from e-waste, such as cyanidation and electrorefining, often suffer from low efficiency and poor selectivity for gold adsorption [12–14]. Additionally, they typically require harsh chemicals and energy-intensive processes [15]. Although some of these methods showed excellent recovery efficiencies in the laboratory, translating these materials from the

lab to real-world conditions remains a substantial challenge [16–18]. The selectivity and efficiency issues with current methods for gold recovery are partly due to the complex mixture of competing metals and the low gold content in e-waste leachate [19–21]. Therefore, there is a growing need for sustainable and environmentally friendly gold recovery technologies with high capacity and excellent selectivity.

Vinyl-linked covalent organic frameworks (v-2D-COFs) [22–26] have emerged as promising semiconductor materials for adsorption and separation applications due to their chemical and structural tunability [26–29], large surface area [30–33], excellent adsorption selectivity [34–36], and stability [25, 37, 38, 39]. In particular, v-2D-COFs offer significant advantages for photocatalysis due to their in-plane conjugation [40, 41] and unique optoelectronic properties [42–48]. Their conjugated electron system can promote interaction with gold ions, while their adjustable functional groups further enhance the selective adsorption of gold ions [23]. However, achieving an optimal balance between selectivity and efficiency remains a critical challenge [15, 49, 50]. Recent studies have shown that incorporating nanotraps into porous frameworks such as COFs can result in high adsorption capacity and selective separation of gold ions, characterized by a relatively low binding affinity [20, 51, 52, 53]. Engineering specific nanotraps along the COF pore walls is a powerful emerging strategy to optimize interactions with gold ions [17], enabling effective and selective adsorption from complex mixtures.

In this study, we investigate the systematic application of three vinyl-azole-bridged highly stable covalent organic frameworks (v-2D-COFs-NS/NO/NN) via aldol polycondensation. The heteroatoms in the azole group form a nanotrap with an electropositive microenvironment, thereby enhancing electrostatic interactions with chloroaurate ions and achieving excellent selectivity for gold. Furthermore, the heteroatomic nanotrap structure creates a nanocaging effect, effectively trapping gold ions and facilitating electron excitation via a photocatalytic process [50], thereby enhancing the reduction of gold ions and their transformation into metallic gold. The v-2D-COFs-NS containing thiazole moieties with N and S atoms achieved a gold recovery of 99.6%, even in complex matrices containing competing metals, such as the dilute acid leachate from discarded Central Processing Units (CPUs). We employed x-ray photoelectron spectroscopy (XPS) and density functional theory (DFT) calculations to elucidate the interaction mechanism between gold ions and the heteroatomic nanotrap of v-2D-COFs, providing a crucial theoretical foundation for the gold recovery process. This work introduces a new class of high-performance COF photocatalysts that feature nanotraps for highly efficient gold recovery.

2 | Results and Discussion

2.1 | Synthesis and Characterization

Leveraging the successful reaction previously reported, three vinylazole-linked COFs (v-2D-COF-NS/NO/NN) were synthesized via an aldol condensation reaction. These COFs possess similar structures and consistent pore sizes, as shown in Figure 1a. Benzene-1,3,5-tri carboxaldehyde (BTCA) and 2,6-dimethyl[1,3]thiazo[5,4-f][1,3]benzothiazole (DTBT) [22] (Figure S1), 2,6-bis(2-phenylethylene)benzo[1,2-b:4,5-b']bisoxazole (BPBO) [24] (Figure S2), and 2,6-dimethyl-1,5-dihydrobenzo[1,2-d: 4,5-d']diimidazole (DBDA) (Figure S3)were heated at 200°C and reacted with phthalic anhydride (BA) as catalyst for 5 days to obtain the corresponding 2D vinyl covalent organic frameworks: v-2D-COF-NS (DTBT), v-2D-COF-NO (BPBO), and v-2D-COF-NN (DBDA).

Fourier transform infrared (FT-IR) spectroscopy results (Figure 1b) confirm the successful conversion of v-2D-COF-NN. The FT-IR spectrum shows the appearance of a ~1624 cm^{-1} band attributed to vinyl bond formation, which is in the v-2D-COF spectra, indicating a high degree of aldol-type condensation. Small-angle x-ray scattering (SAXS) was used to examine the structural properties of the materials. The 1D I-2θ curves (Figure S4c,d), derived from the azimuthal integration of the 2D-SAXS images (Figure S4a,b), showed good agreement with the simulated AA stacking spectra in terms of peak positions and relative intensities. This confirms the highly ordered structures of v-2D-COF-NS and v-2D-COF-NO and validates the structural model used. Although the crystal structure of v-2D-COF-NN remains elusive, it shows no distinct diffraction features that would allow for meaningful evaluation of long-range crystallinity under the current synthesis conditions. As a result, its crystallinity is considered limited, and diffraction-based structural refinement is not pursued. However, this limitation does not affect the material's performance, as Au(III) capture and photoreduction are primarily governed by local heteroatom coordination and the nanotrap microenvironment, rather than long-range periodicity. FTIR data for v-2D-COF-NN after immersion in strong acid (6 M HCl), strong base (6 M NaOH), and a mixture of organic solvents (acetone and THF) for 72 h (Figure S5) show that the material maintains excellent chemical stability under these extreme conditions.

N_2 adsorption measurements show that v-2D-COF-NS/NO/NN have BET surface areas of 369, 189, and 242 $m^2\ g^{-1}$ (Figure 1c), the moderate values likely arise from drying/activation-induced pore shrinkage and nanosheet restacking, which reduce gas accessibility. Notably, N_2-BET at 77 K reflects dry-state gas-accessible porosity and is not a direct proxy for aqueous $AuCl_4^-$ capture. For $AuCl_4^-$ adsorption and photocatalytic enrichment in aqueous media, performance is governed by the external surface area of thin nanosheets and the heteroatom-rich nanotrap microenvironment that concentrates $AuCl_4^-$ and promotes coordination-assisted electron transfer, consistent with the rapid uptake and high capacities observed for all three COFs. Nonlocal density functional theory (NLDFT) analysis indicates pore sizes centered around ~1.9 nm for all three materials, consistent with theoretical models (Figure 1d). Minor larger-pore signals arise from structural defects and loose chain packing.

The microstructure of the v-2D-COF materials was investigated using transmission electron microscopy (TEM), which revealed a well-defined layered structure. Energy-dispersive x-ray spectroscopy (EDS) further confirmed the elemental composition of the materials (Figures S6–S8). These combined results provide strong evidence for the successful formation of v-2D-COF-NS/NO/NN.

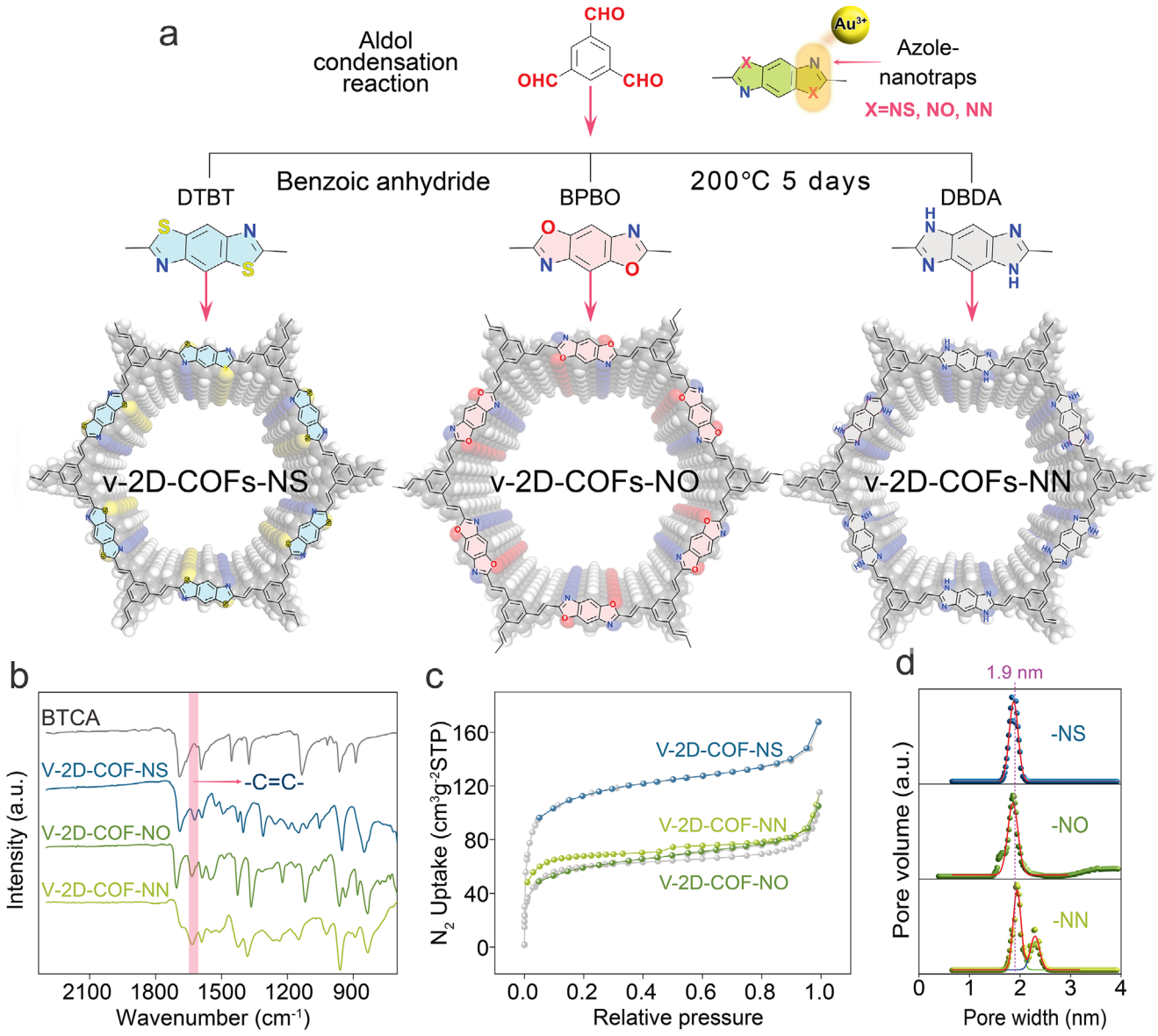

FIGURE 1 | Schematic diagram of the synthesis of v-2D-COFs and their use for gold recovery. (a) v-2D-COF-NS, v-2D-COF-NO and v-2D-COF-NN were synthesized by aldol polymerization of benzene-1,3,5-tricarbaldehyde (BTCA) with 2,6-dimethyl[1,3]thiazolo[5,4-f][1,3]benzothiazole (DTBT), 2,6-bis(2-phenylethenyl)benzo[1,2-b:4,5-b′]bisoxazole (BPBO) and 2,6-dimethyl-1,5-dihydrobenzo[1,2-d:4,5-d′]diimidazole (DBDA). (b) FT-IR spectra of BTCA (gray line), v-2D-COF-NS (blue line), v-2D-COF-NO (green line), and v-2D-COF-NN (light green line). (c,d) N_2 adsorption isotherm (c) and pore size distribution (d).

2.2 | Adsorption Performance

We investigated the adsorption kinetics of v-2D-COF-NS/NO/NN using inductively coupled plasma optical emission spectroscopy (ICP-OES) at 298K under visible-light irradiation at an oscillation speed of 600 rpm/min. We specifically examined the adsorption behavior over different contact times (0–6 h) and at an initial concentration of 10 ppm. Kinetic studies showed that v-2D-COF-NS reaches adsorption saturation within 1.5 h, and its adsorption process better fits the pseudo-first-order kinetic model (Figure 2a). In contrast, v-2D-COF-NO and v-2D-COF-NN reach saturation at 2 and 3 h, respectively. The adsorption behavior of v-2D-COF-NO follows the pseudo-second-order kinetic model (Figure 2b), while v-2D-COF-NN fits the pseudo-first-order kinetic model (Figure 2c). Additionally, under high-concentration, low-volume conditions, all three materials can achieve nearly 100% gold-ion removal within 30 min (Figure S9). Furthermore, we investigated the impact of pH value and light conditions on adsorption performance. A 5 mg v-2D-COFs adsorbent was reacted with 100 mL of a 10 ppm Au(III) solution for 180 min under both dark and xenon light irradiation. Since v-2D-COF-NS shows a positive zeta potential under low pH conditions (Figure S10), it demonstrates optimal adsorption performance at pH = *3* (Figure 2d). The optimal adsorption pH for v-2D-COF-NO and v-2D-COF-NN were found to be 5–6 and 2, respectively (Figure S11).

We assessed the adsorption performance of v-2D-COFs for noble metal ions by measuring the adsorption isotherms of v-2D-COFs in Au^{3+} solutions with concentrations

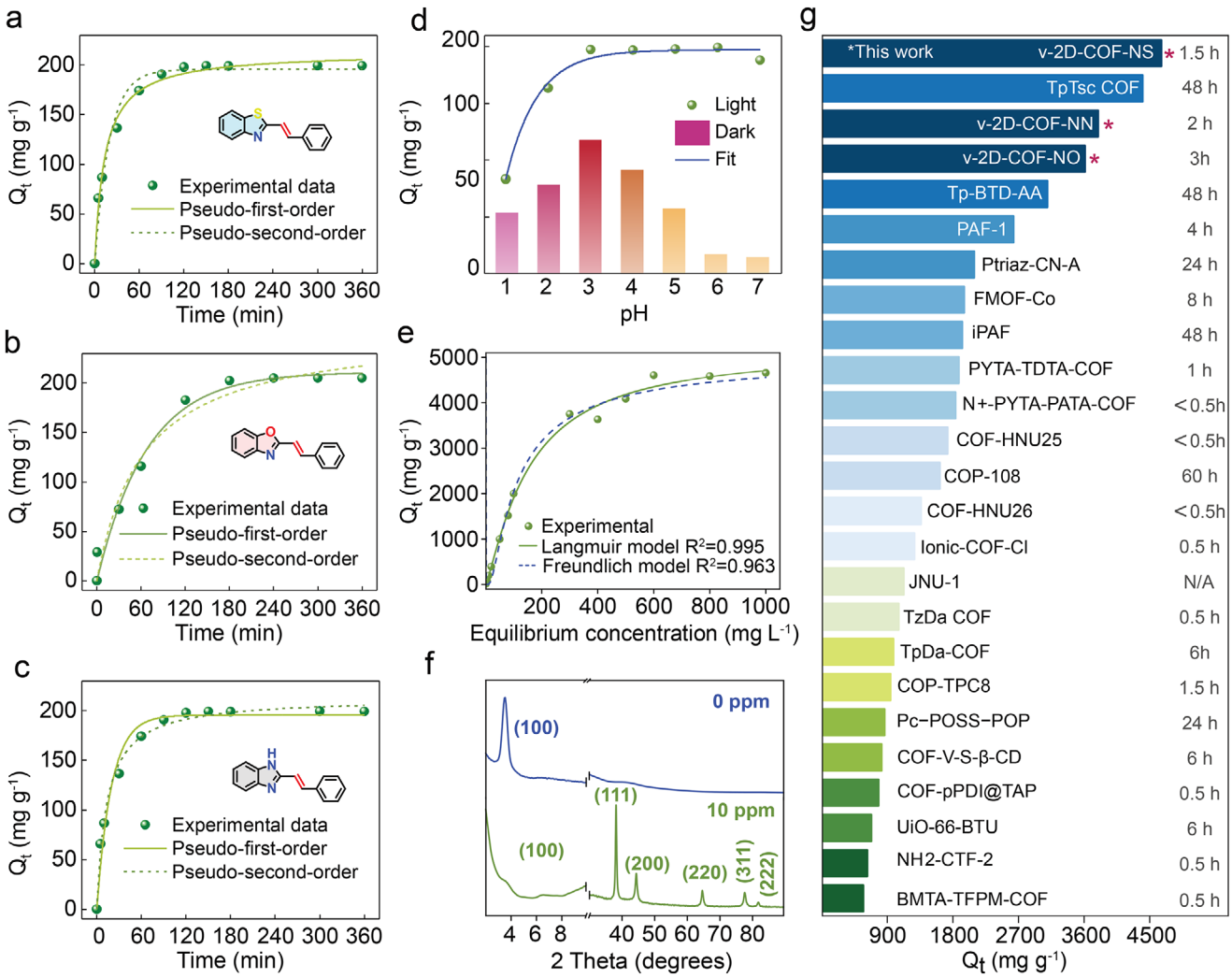

FIGURE 2 | Adsorption performance of v-2D-COFs. (a–c) Adsorption kinetics of Au^{3+} ions obtained under visible light for v-2D-COF-NS (a), v-2D-COF-NO (b), and v-2D-COF-NN (c). (d) Effect of pH on the amount of gold ions adsorbed per unit mass of adsorbent at equilibrium ($mg{\cdot}g^{-1}$) (Q_e) of v-2D-COF-NS under light and dark conditions. (e) Adsorption isotherms of v-2D-COF-NS fitted with the Langmuir and the Freundlich models. (f) x-ray diffraction (XRD) patterns of v-2D-COF-NS before and after Au^{3+} adsorption. (g) Adsorption capacity of our COF materials (*) compared with other representative porous adsorbents (e.g., COFs, MOFs, etc.) reported in the literature (Data *source*: Table S1).

ranging from 1 to 1000 ppm. To ensure adsorption equilibrium, the solution was stirred under light conditions for 3 h, followed by filtration. The residual Au^{3+} concentration in the solution was then quantified using ICP-OES. As the initial gold ion concentration increased, the adsorption amount progressively rose and eventually plateaued (Figure 2e). Among the materials tested, v-2D-COF-NS exhibited the highest gold adsorption capacity, with a maximum adsorption capacity of 4.6581 $g{\cdot}g^{-1}$, surpassing v-2D-COF-NN (3.7898 $g{\cdot}g^{-1}$) and v-2D-COF-NO (3.6106 $g{\cdot}g^{-1}$), all of which exceed the adsorption capacities reported for most porous organic polymer materials (Figure 2g and Table S1). The experimental data were fitted to both the Freundlich and Langmuir adsorption isotherm models. The results indicate that the Langmuir model provides a better description of the equilibrium adsorption behavior of v-2D-COFs (Figure 2e and Figure S12), suggesting that the adsorption of gold ions follows a monolayer adsorption mechanism. This process involves both physical and chemical adsorption, further confirming the presence of a synergistic adsorption mechanism during the photocatalytic gold extraction process.

The PXRD spectra in Figure 2f were recorded from a v-2D-COFs-NS adsorbent before and after adsorption experiments with visible light. These result shows crystal plane peaks from metallic Au (111), (200), (220), (311), and (222) at 2θ values of 38.18°, 44.39°, 64.58°, 77.55°, and 81.72° (Figure 2f), indicating that during the adsorption process, Au (III) was indeed adsorbed by V-2D-COFs-NS and reduced to Au(0). The v-2D-COF-NS morphology comparison before and after adsorption in Figure 3b,c shows that a new phase with uniform distribution is generated in the v-2D-COF-NS-Au composite, as shown by the uniformly distributed particles in Figure 3c. The HRTEM image of the new phase shows that its particle size is about 5 nm and the lattice spacing is 2.4 Å, which is consistent with the theoretical spacing of the Au(0) (111) plane, indicating that the new phase generated after adsorption is Au(0) (Figure 3d), in agreement with XRD results. Both SEM and TEM imaging demonstrate a uniform distribution of Au(0),

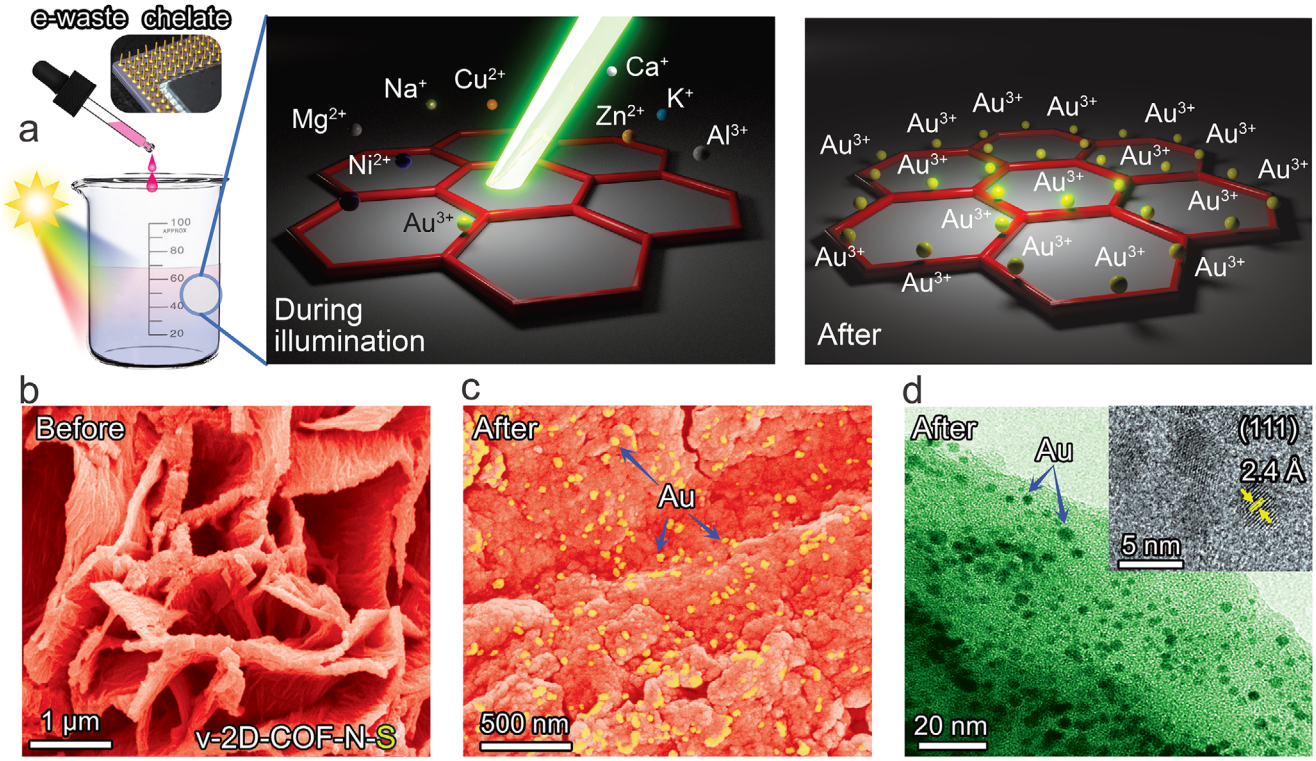

FIGURE 3 | Morphology of v-2D-COFs before and after adsorption. a Schematic diagram of the wet chemical method for gold recovery from electronic waste using v-2D-COFs. b,c SEM image of v-2D-COF-NS before reaction (b) and after reaction (c). d HR-TEM image of v-2D-COF-NS after reaction.

which can be attributed to the inherently high porosity of the COF. In addition, the SEM image of v-2D-COF-NO after gold adsorption further confirms this uniform distribution (Figure S13). TEM images of v-2D-COF-NO/NN after gold adsorption (Figures S14 and S16), in conjunction with EDS analysis (Figures S15 and S17), provide additional evidence for the homogeneous dispersion of gold. In conclusion, these results unequivocally demonstrate that v-2D-COF-NS effectively facilitates the in-situ adsorption and reduction of Au^{3+} to Au^{0} under visible light irradiation.

2.3 | Optical Properties

The photochemical properties of v-2D-COF-NS, v-2D-COF-NO, and v-2D-COF-NN were systematically investigated using multiple spectroscopic techniques. Ultraviolet-visible (UV–vis) absorption spectra (Figure S18) revealed that all three COFs exhibit broad absorption ranges extending from the visible to the near-infrared region, with optical bandgaps of 1.73 eV (v-2D-COF-NS), 1.70 eV (v-2D-COF-NO), and 1.26 eV (v-2D-COF-NN), indicating their strong potential for visible-light-responsive photocatalytic applications (Figure S19). Further ultraviolet photoelectron spectroscopy (UPS) analysis (Figures S20 and S21) confirmed the rational band structures of the COFs, with valence and conduction band positions conducive to the electron transfer processes required for photocatalytic reactions. In addition, photoluminescence (PL) spectra (Figure S22) showed that all three materials exhibit efficient photogenerated charge separation, which suppresses carrier recombination and enhances photocatalytic efficiency.

2.4 | Adsorption Mechanism

To further elucidate the details behind the transformation mechanism, we performed XPS analysis of v-2D-COFs with and without Au adsorption. In the XPS spectrum of the v-2D-COF-NS sample without Au adsorption, only the characteristic peaks of C 1s, O 1s, N 1s, and S 2p were detected, indicating that these elements constitute the framework structure of the pristine v-2D-COFs material. However, after Au adsorption, the characteristic peak of Au 4f was clearly observed alongside the original element peaks, providing direct evidence that Au was successfully adsorbed onto the surface of the v-2D-COFs (Figure S23). A further comparison of the XPS spectra for v-2D-COF-NO and v-2D-COF-NN after Au adsorption (Figure S24) revealed the consistent appearance of Au 4f peaks across all samples. These peaks indicate that Au is predominantly in its metallic state during adsorption. Moreover, the uniform intensity and distribution of the Au 4f peaks suggest that Au is evenly adsorbed on the surfaces of each sample, confirming the successful and stable incorporation of Au into the v-2D-COFs structures. This finding is consistent with Energy-dispersive x-ray spectroscopy (EDS), confirming the successful adsorption of Au(III) by v-2D-COFs.

The fitted XPS spectrum in Figure 4b demonstrates that after v-2D-COF-NS adsorbs Au^{3+} in aqueous solutions at different concentrations, the two oxidation states of gold, Au 4f7/2 and Au 4f5/2, are detected. At the lowest Au^{3+} concentration of 10 ppm, the Au 4f peak splits into four peaks corresponding to Au(0): Au 4f5/2 (87.42 eV) and Au 4f7/2 (84.30 eV), and Au^{1+}: Au 4f5/2 (88.15 eV) and Au 4f7/2 (84.75 eV). However, at a higher 1000 ppm Au^{3+} concentration, the v-2D-COF-NS@Au XPS

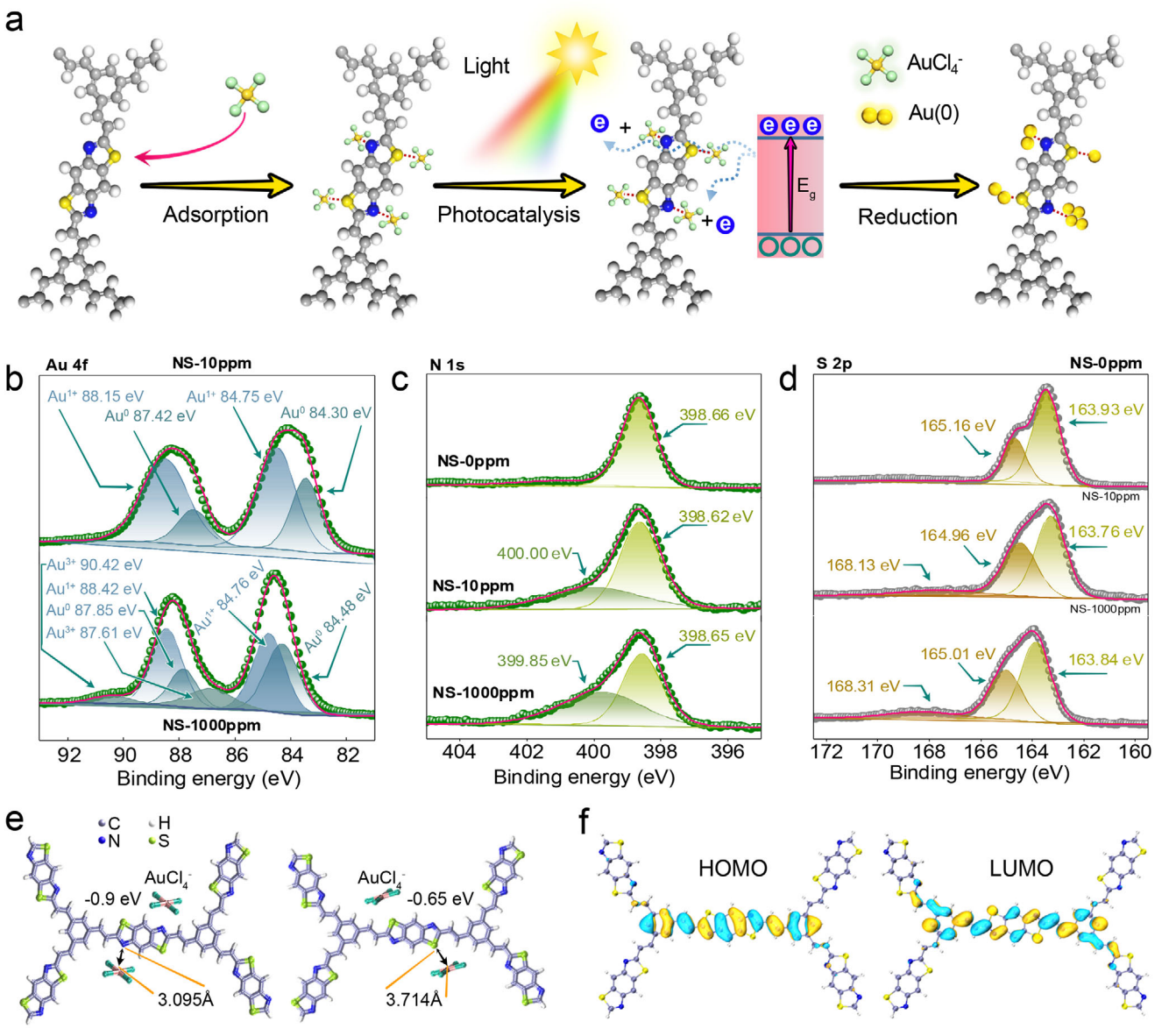

FIGURE 4 | Analysis of the binding interaction between v-2D-COF-NS and gold ions. a Mechanism diagram of photocatalytic gold extraction. b-d XPS spectra of Au 4f (b), N 1s (c) and S 2p (d) of v-2D-COF-NS under light. (e) Interaction energies between $AuCl_4^-$ and the azole-based framework in v-2D-COFs. f Frontier molecular orbital distribution of v-2D-COFs. The colored shading represents the integrated area of different characteristic peaks.

spectrum reveals three oxidation states: Au(0) at 87.85 eV (4f5/2) and 84.48 eV (4f7/2), Au^{1+} at 88.42 eV (4f5/2) and 84.76 eV (4f7/2), and Au^{3+} at 90.42 eV (4f5/2) and 87.61 eV (4f7/2) (Figure 4d). Similarly, the XPS spectra of v-2D-COF-NO@Au and v-2D-COF-NN@Au at a concentration of 200 ppm also exhibit three oxidation states (Figure S25). These results indicate that chelation and photocatalytic reduction reactions occurred between Au(III) and the adsorbent.

Moreover, at low Au^{3+} concentrations, the v-2D-COFs adsorbent promptly reduces adsorbed Au^{3+} to Au^{1+} and Au(0) via photogenerated electrons. At higher concentrations, the adsorbent undergoes photoreduction during adsorption, continuously exposing active sites to adsorb further and reduce Au^{3+}. This cycle repeats until the generated Au(0) crystals grow large enough to cover all available active sites, in agreement with the post-reaction XRD analysis. To better understand the interaction between Au^{3+} and v-2D-COFs, we compared the XPS N 1s, O 1s, and S 2p spectra of v-2D-COFs and v-2D-COFs@Au, allowing us to investigate the actual active adsorption sites of v-2D-COF-NS. In the XPS N 1s spectrum of v-2D-COF-NS, a single peak is observed at 398.66 eV (C═N) prior to adsorption. Upon adsorption, this peak shifts, and an N-metal peak emerges at 400 eV (Figure 4c). Similarly, in the XPS spectrum of N 1s for v-2D-COF-NO, only a C═N bond peak is present before adsorption, but an N-metal peak appears at 400.05 eV after adsorption. However, for v-2D-COF-NN, the C═N (398.98 eV) and C—N (400.03 eV) bond peaks merely shift without forming any new peaks (Figure S26). This behavior is attributed to lone-pair electrons on the nitrogen atom, which form a shared bond with the Au ion, decreasing the electron cloud density around the nitrogen atom and increasing the binding energy. This indicates that the nitrogen-containing functional group effectively chelates with Au(III). For the O 1s XPS spectrum in

v-2D-COF-NO, the peak was simply shifted, forming a shared bond with the gold ions (Figure S27). Furthermore, the new peak at 168.31 eV in the S 2p spectrum of v-2D-COF-NS-Au displays a similar interaction between Au^{3+} ions and sulfur atoms (Figure 4d).

2.5 | DFT Calculation

In v-2D-COF-NS, the reduction of $AuCl_4^-$ primarily occurs through coordination with N and S atoms in the benzothiazole group (Figure 4e). Specifically, the gold atom coordinated with the thiazole N atom exhibits the highest binding energy (−2.07 eV) with a bond length of 2.45 Å. The gold atom coordinated to the S atom exhibits a slightly lower binding energy (−0.65 eV) and a bond length of 3.71 Å. These results indicate that both N and S atoms serve as critical active sites for electron transfer, with N atoms showing higher binding strength and contributing more significantly to the gold reduction process. The distribution of active sites in different v-2D-COFs was further validated through electron spin polarization (ESP) maps (Figure S28). For v-2D-COF-NS, the electron polarization is predominantly localized on the N and S atoms within the benzothiazole group. In contrast, v-2D-COF-NO and v-2D-COF-NN exhibit slightly different electron-polarization distributions due to their distinct linking groups; however, both still exhibit clear coordination activity. Combined with the molecular orbital distribution diagrams (Figures S29–S31), the lowest unoccupied molecular orbitals (LUMO) of the v-2D-COFs are shown to primarily originate from the benzothiazole, benzoxazole, and benzimidazole groups. These findings confirm that these groups are the principal active regions for electron transfer during photocatalysis. Furthermore, the analysis of Figure 4f reveals that, in v-2D-COF-NS, photogenerated electrons are efficiently transferred to $AuCl_4^-$ through N and S atoms, enabling its reduction to metallic Au(0). This demonstrates that v-2D-COF-NS possesses distinct advantages in the photocatalytic reduction of Au^{3+}, as its benzothiazole group provides both high binding affinity and stable electron-transfer pathways, thereby enhancing catalytic efficiency. Theoretical insights effectively complement and corroborate the experimental XPS findings discussed earlier. DFT results reveal charge transfer from nitrogen and sulfur atoms to the gold ion, while the observed upshifts in N1s and S2p XPS peaks indicate electron deficiency, confirming the role of these atoms in chelation and photoreduction [23].

2.6 | Gold Recovery From E-Waste

Finally, we focus on illustrating the actual performance of our v-2D-COF adsorbent in the selective extraction of gold under more realistic conditions (Figure 5a). This is a critical application for sustainable gold recycling from waste electrical and electronic equipment (e-waste). In this experiment, e-waste was leached from aqua regia, placed at room temperature for 12 h, and adjusted to pH = *3*. The solution was then filtered through a 0.2 μm membrane, and the metal content of the solution was measured by ICP-OES (Figure S32). Since Cu^{2+} and Ni^{2+} are the two major competing ions in microelectronic components, it is essential to ensure the selectivity of adsorbents toward gold for its recovery from e-waste (Figure S33).

To quantify this selectivity, we investigated Au(III) adsorption by v-2D-COFs-NS from a simulated e-waste solution containing 10 ppm of Au^{3+} ions and 100 ppm of several competing ions (Cu^{2+}, Ni^{2+}, Mg^{2+}, Al^{3+}, Zn^{2+}, K^+, Na^+, Ca^{2+}) as illustrated in Figure 5a. The recovery rate R(%) results in Figure 5b show a remarkable preferential adsorption for gold, reaching a record-high recovery of 99.6% with a negligible capture of competing ions (< 2%). The v-2D-COF-NS shows an excellent affinity for Au(III) (Figures S34 and S35), even when many competing ions are present at concentrations one order of magnitude higher. Furthermore, v-2D-COF-NS can effectively remove nearly all Au^{3+} ions even in the presence of anions such as F^-, Br^-, NO_3^-, SO_4^{2-}, and PO_4^{3-}, while the adsorption of these anions remains negligible, further emphasizing its exceptional selectivity for Au(III) (Figure S36).

Excited by these results, we further investigated the performance of our v-2D-COFs-NS material in actual e-waste leachate, which contains a much higher concentration of the competing copper ion (5265.4 mg/mL) and only trace levels of gold (42.4 mg/mL). After 6 h of illumination, the recovery rate for trace gold remained remarkably high at 99.2%. In contrast, results in Figure 5c show that, despite the large excess of copper ions, their removal reached only 25% (corresponding to a large absolute mass, given their high concentration). Near-total recovery of gold demonstrates our material's strong affinity for this metal, as further confirmed by post-adsorption SEM-EDS analysis results in Figure 5d.

There are two reasons for this remarkable selectivity. First, from the point of electrostatic interactions, in low pH solutions, the positively charged v-2D-COFs-NS is more conducive to the removal of Au(III) anions in the form of the $AuCl_4^-$ complex due to electrostatic attraction. This situation contrasts with that of Cu^{2+} and Ni^{2+}, which, due to their positive charges, are subject to electrostatic repulsion that hinders adsorption. Second, the standard electrode potentials of $Cu^{2+}|Cu$, $Ni^{2+}|Ni$, $Mg^{2+}|Mg$, $Al^{3+}|Al$ and Au(III)| Au(0) are +0.34, −0.23, −2.37, −1.66 and +1.50 V. This shows that the electrophilicity of metal ions such as Cu^{2+}, Ni^{2+}, Mg^{2+}, and Al^{3+} is much lower than that of Au(III) ions. Hence, the reduction potentials of Cu^{2+} and Ni^{2+} during adsorption are almost negligible. The results show that v-2D-COFs-NS is an efficient and selective adsorbent for recovering gold from e-waste leachate containing base metals.

The material also demonstrated excellent cyclic stability. As shown in Figure S37, after desorption using thiourea, v-2D-COF-NS maintained high gold removal and recovery rate over five consecutive adsorption-desorption cycles. This robust photocatalytic performance is due to the nature of the redox pair. The energy band analysis in Figure S21 shows that the valence band maximum (V_{BM}) of our COFs (−5.30 to −5.84 eV; −1.34 to −0.80 V vs. NHE) is significantly more negative than the oxidation potentials of water and chloride, making these reactions thermodynamically unfavorable. This was confirmed experimentally using highly sensitive colorimetric assays; neither H_2O_2 (with potassium titanium oxalate) nor hypochlorous acid (with N,N-diethyl-p-phenylenediamine) were detected, showing that photogenerated holes do not oxidize the solvent [23]. Instead, the COF framework itself serves as the

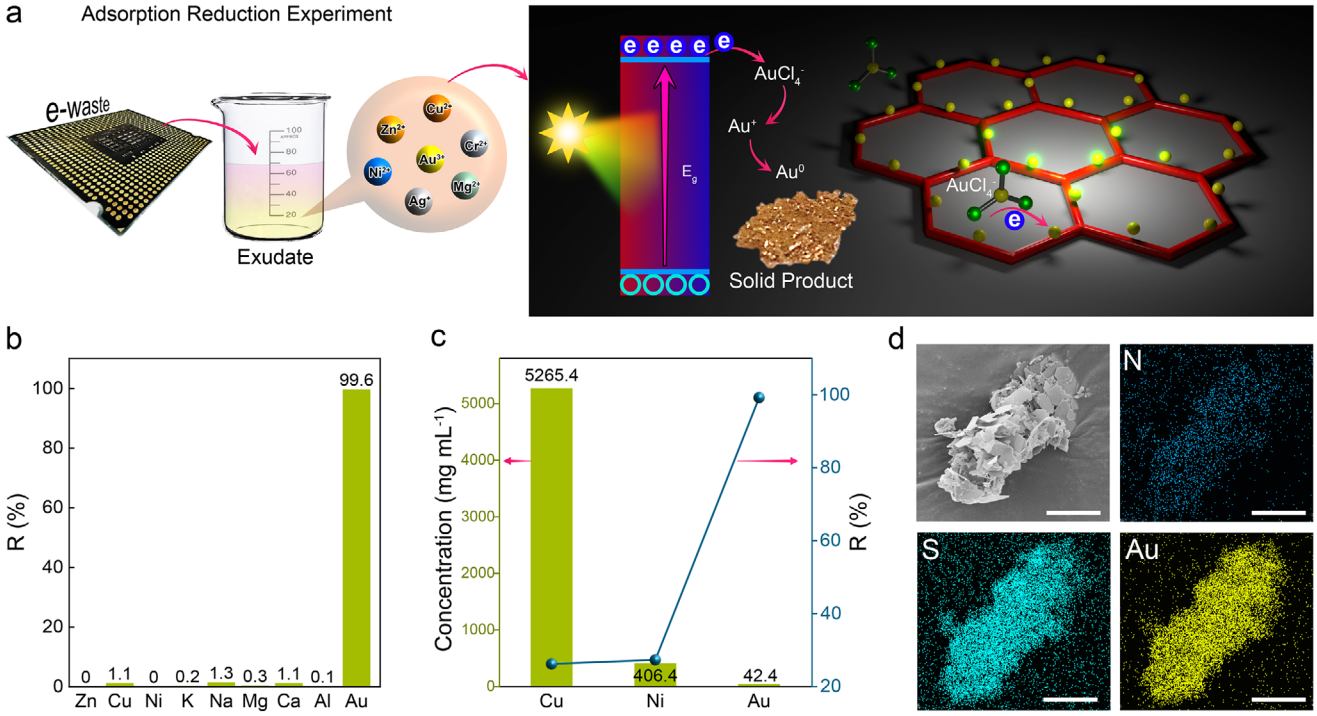

FIGURE 5 | Extraction of gold from e-waste leachate by v-2D-COF-NS. (a) Flow chart of gold extraction from e-waste by v-2D-COF-NS. (b) Recovery rate (R%) of v-2D-COFs-NS for various metal ions, including Zn, Cu, Ni, K, Na, Mg, Ca, Al, and Au, from mixed metal ion solution. (c) Adsorption capacity (mg/mL) and recovery rate (R%) of v-2D-COFs-NS for Cu, Ni, and Au from e-waste leachate. (d) Elemental analysis of gold recovered from e-waste leachate by v-2D-COF-NS. The scale bar is 3 μm.

electron donor in a partly reversible process. FTIR spectroscopy (Figure S38a–f) directly showed the oxidation of C═C to C═O groups, evidenced by the attenuation of the 1620 cm^{-1} peak and a shift at 1700 cm^{-1} during adsorption, with partial recovery of the C═C signal after desorption, confirming the framework's stability.

To eliminate potential interference from the spontaneous reduction of gold ions under light, blank control experiments were conducted (Table S2 and Figure S39). The results revealed that in the absence of the catalyst, spontaneous reduction of gold ions was minimal (≤20%) even after 24 h of light exposure. This reduction was far lower than the efficiency and rate observed with the COF material, confirming that v-2D-COF-NS is primarily responsible for the photocatalytic reduction of gold.

3 | Conclusion

In summary, we have synthesized three vinyl-benzazole-bridged covalent organic frameworks (v-2D-COF-NS/NO/NN) through azole-mediated aldol condensation polymerization. The strategic incorporation of various azole groups creates nanotraps within the COF pores, which show high responsiveness to gold ion adsorption through size selectivity and electrostatic interactions with chloroaurate ions. The heteroatoms within the azole groups create an electropositive microenvironment, further enhancing gold adsorption and nanocage locking. Notably, v-2D-COF-NS achieves a high gold ion adsorption capacity of 4.6581 g g^{-1} under visible-light irradiation in optimal conditions and successfully recovered 99.2% of gold from real-world e-waste leachates, even in the presence of high concentrations of competing ions. This work highlights the synergy between the engineered azole-based nanotraps and the photocatalytic activity of v-2D-COFs for selective and efficient gold recovery.

Author Contributions

T.Z. and S.W. conceived the project and methodology, Q.Y. performed the experiments and structural characterization. J.H. and W.Z. performed the DFT calculations. S.L. contributed to the structural characterization. M.C. and J.H. advised on the results. All authors participated in the discussion and approved the final manuscript version. Q.Y., R.D.R., and T.Z. co-wrote the manuscript, including graphics and visualizations.

Acknowledgements

T. Zhang acknowledges the support from the National Natural Science Funds for Excellent Young Scholars (Grant No. 51322315) and the Natural Science Foundation of Zhejiang Province (Grant No. LRG 25E03 0001); International Cooperation and Exchanges Programme of Ningbo (Grant No. 2024H024); and TPU Priority 2030. T. Zhang acknowledges the National Natural Science Fund for Excellent Young Scholars (Grant No. 52322316), the Leading Innovative and Entrepreneur Team Introduction Program of Zhejiang (2021R01005), the Key Research and Development Program of Ningbo (2022ZDYF020023), and TPU Priority 2030.

Conflicts of Interest

The authors declare no conflict of interest.

Data Availability Statement

The experimental and theoretical data that support the findings of this study are available from the corresponding authors upon reasonable request.

References

1. P. Peng and A. Shehabi, "Regional Economic Potential for Recycling Consumer Waste Electronics in the United States," *Nature Sustainability* 6, no. 1 (2023): 93–102, https://doi.org/10.1038/s41893-022-00983-9.

2. M. Eisenstein, "Upgrading The Electronics Ecosystem," *Nature* 611 (2022): S8–S10.

3. A. K. Awasthi, J. Li, L. Koh, and O. A. Ogunseitan, "Circular Economy and Electronic Waste," *Nature Electronics* 2 (2019): 86–89, https://doi.org/10.1038/s41928-019-0225-2.

4. "Electronics can be More Sustainable," *Nature Materials* 22 (2023): 1273, https://doi.org/10.1038/s41563-023-01731-w.

5. "The Materials We Make Don't Just Go 'away'," *Nature Reviews Materials* 10 (2025): 713–714, https://doi.org/10.1038/s41578-025-00845-8.

6. P. Wang, L.-Y. Zhang, A. Tzachor, and W.-Q. Chen, "E-waste Challenges of Generative Artificial Intelligence," *Nature Computational Science* 4 (2024): 818–823, https://doi.org/10.1038/s43588-024-00712-6.

7. C. P. Baldé, R. Kuehr, T. Yamamoto, et al., *The Global E-Waste Monitor 2024* (International Telecommunication Union, 2024), https://www.itu.int/en/ITU-D/Environment/Pages/Publications/The-Global-E-waste-Monitor-2024.aspx.

8. M. Takakuwa, K. Fukuda, T. Yokota, et al., "Direct Gold Bonding for Flexible Integrated Electronics," *Science Advances* 7 (2021): abl6228, https://doi.org/10.1126/sciadv.abl6228.

9. Y.-C. Lu, Z. Xu, H. A. Gasteiger, S. Chen, K. Hamad-Schifferli, and Y. Shao-Horn, "Platinum−Gold Nanoparticles: A Highly Active Bifunctional Electrocatalyst for Rechargeable Lithium−Air Batteries," *Journal of the American Chemical Society* 132 (2010): 12170–12171, https://doi.org/10.1021/ja1036572.

10. T. W. Van Deelen, C. Hernández Mejía, and K. P. De Jong, "Control of Metal-Support Interactions in Heterogeneous Catalysts to Enhance Activity and Selectivity," *Nature Catalysis* 2 (2019): 955–970, https://doi.org/10.1038/s41929-019-0364-x.

11. A. Zadehnazari, F. Auras, A. A. Altaf, et al., "Recycling E-Waste Into Gold-Loaded Covalent Organic Framework Catalysts for Terminal Alkyne Carboxylation," *Nature Communications* 15 (2024): 10846, https://doi.org/10.1038/s41467-024-55156-3.

12. H. Mahandra, F. Faraji, and A. Ghahreman, "Novel Extraction Process for Gold Recovery From Thiosulfate Solution Using Phosphonium Ionic Liquids," *ACS Sustainable Chemistry & Engineering* 9 (2021): 8179–8185, https://doi.org/10.1021/acssuschemeng.1c01705.

13. N. A. A. Qasem, R. H. Mohammed, and D. U. Lawal, "Removal of Heavy Metal Ions From Wastewater: A Comprehensive and Critical Review," *npj Clean Water* 4 (2021): 36, https://doi.org/10.1038/s41545-021-00127-0.

14. Q. Xu, X.-H. Du, D. Luo, M. Strømme, Q.-F. Zhang, and C. Xu, "Gold Recovery From E-Waste Using Freestanding Nanopapers of Cellulose and Ionic Covalent Organic Frameworks," *Chemical Engineering Journal* 458 (2023): 141498, https://doi.org/10.1016/j.cej.2023.141498.

15. K. Vaca-Escobar, D. Arregui-Almeida, and P. Espinoza-Montero, "Chemical, Ecotoxicological Characteristics, Environmental Fate, and Treatment Methods Applied to Cyanide-Containing Wastewater," *npj Clean Water* 7 (2024): 103, https://doi.org/10.1038/s41545-024-00392-9.

16. T. Ma, R. Zhao, Z. Li, et al., "Efficient Gold Recovery From E-Waste via a Chelate-Containing Porous Aromatic Framework," *ACS Applied Materials & Interfaces* 12 (2020): 30474–30482, https://doi.org/10.1021/acsami.0c08352.

17. X. Li, Y.-L. Wang, J. Wen, et al., "Porous Organic Polycarbene Nanotrap for Efficient and Selective Gold Stripping From Electronic Waste," *Nature Communications* 14 (2023): 263, https://doi.org/10.1038/s41467-023-35971-w.

18. Y. Hong, D. Thirion, S. Subramanian, et al., "Precious Metal Recovery From Electronic Waste by a Porous Porphyrin Polymer," *Proceedings of the National Academy of Sciences* 117 (2020): 16174–16180, https://doi.org/10.1073/pnas.2000606117.

19. J. Guo, X. Fan, J. Wang, et al., "Highly Efficient and Selective Recovery of Au(III) From Aqueous Solution by Bisthiourea Immobilized UiO-66-NH_2: Performance and Mechanisms," *Chemical Engineering Journal* 425 (2021): 130588, https://doi.org/10.1016/j.cej.2021.130588.

20. D. Mei and B. Yan, "A 2D Acridine-Based Covalent Organic Framework for Selective Detection and Efficient Extraction of Gold From Complex Aqueous-Based Matrices," *Angewandte Chemie International Edition* 63 (2024): 202402205.

21. J. Liu, Z. Deng, H. Yu, and L. Wang, "Ferrocene-Based Metal-Organic Framework for Highly Efficient Recovery of Gold From WEEE," *Chemical Engineering Journal* 410 (2021): 128360, https://doi.org/10.1016/j.cej.2020.128360.

22. S. Li, R. Ma, S. Xu, et al., "Two-Dimensional Benzobisthiazole-Vinylene-Linked Covalent Organic Frameworks Outperform One-Dimensional Counterparts in Photocatalysis," *ACS Catalysis* 13 (2023): 1089–1096, https://doi.org/10.1021/acscatal.2c05023.

23. Q. Yang, J. Han, S. Li, M. Chen, S. Wang, and T. Zhang, "Isomeric π Conjugated Covalent Organic Frameworks with Tunable Nitrogen Topologies for Integrated Gold Adsorption and Photoreduction," *Angewandte Chemie International Edition* 137 (2025): 202516067.

24. S. Li, R. Ma, S. Xu, et al., "Direct Construction of Isomeric Benzobisoxazole–Vinylene-Linked Covalent Organic Frameworks With Distinct Photocatalytic Properties," *Journal of the American Chemical Society* 144 (2022): 13953–13960, https://doi.org/10.1021/jacs.2c06042.

25. G. Fu, D. Yang, S. Xu, et al., "Construction of Thiadiazole-Bridged sp^2 -Carbon-Conjugated Covalent Organic Frameworks With Diminished Excitation Binding Energy Toward Superior Photocatalysis," *Journal of the American Chemical Society* 146 (2024): 1318–1325, https://doi.org/10.1021/jacs.3c08755.

26. B. Qi, R. Shen, Z. Ke, et al., "2D sp^2 Carbon-Conjugated Covalent Organic Frameworks: Photocatalytic Platforms for Solar Energy Conversion," *Rare Metals* 44 (2025): 1–45, https://doi.org/10.1007/s12598-025-03604-4.

27. R. Shen, J. Xing, Q. Yue, et al., "Topological Covalent Organic Frameworks for Sustainable Photocatalysis," *Science China Materials* 68 (2025): 3925–3954, https://doi.org/10.1007/s40843-025-3573-5.

28. A. Zadehnazari, A. Khosropour, A. A. Altaf, A. S. Rosen, and A. Abbaspourrad, "Tetrazine-Linked Covalent Organic Frameworks With Acid Sensing and Photocatalytic Activity," *Advanced Materials* 36 (2023): 2311042.

29. A. Acharjya, P. Pachfule, J. Roeser, F. Schmitt, and A. Thomas, "Vinylene-Linked Covalent Organic Frameworks by Base-Catalyzed Aldol Condensation," *Angewandte Chemie International Edition* 58 (2019): 14865–14870, https://doi.org/10.1002/anie.201905886.

30. H. Dong, C. Qu, C. Li, et al., "Recent Advances of Covalent Organic Frameworks-Based Photocatalysts: Principles, Designs, and Applications," *Chinese Journal of Catalysis* 70 (2025): 142–206, https://doi.org/10.1016/S1872-2067(24)60184-1.

31. H. L. Nguyen, "Covalent Organic Frameworks for Atmospheric Water Harvesting," *Advanced Materials* 35 (2023): 2300018, https://doi.org/10.1002/adma.202300018.

32. S. Bi, F. Meng, D. Wu, and F. Zhang, "Synthesis of Vinylene-Linked Covalent Organic Frameworks by Monomer Self-Catalyzed Activation of Knoevenagel Condensation," *Journal of the American Chemical Society* 144 (2022): 3653–3659, https://doi.org/10.1021/jacs.1c12902.

33. C. Ji, H. Shao, Y. Pu, et al., "2D Open Framework Materials: Chemistry, Materials, and Applications," *Advanced Materials* 37 (2025): 13499, https://doi.org/10.1002/adma.202513499.

34. N. M. Alamgir, A. Ahmad, J. K. E. Erum, et al., "Shaping the Future of Solar-Driven Photocatalysis by Reticular Framework Materials," *Journal of Materials Science & Technology* 231 (2025): 193–244, https://doi.org/10.1016/j.jmst.2025.02.009.

35. Z. Zhang, C. Kang, S. B. Peh, et al., "Efficient Adsorption of Acetylene Over CO_2 in Bioinspired Covalent Organic Frameworks," *Journal of the American Chemical Society* 144 (2022): 14992–14996, https://doi.org/10.1021/jacs.2c05309.

36. T. Liu, Y. Zhao, M. Song, et al., "Ordered Macro–Microporous Single Crystals of Covalent Organic Frameworks With Efficient Sorption of Iodine," *Journal of the American Chemical Society* 145 (2023): 2544–2552, https://doi.org/10.1021/jacs.2c12284.

37. T. Wang, B. Tian, B. Han, et al., "Recent Advances on Porous Materials for Synergetic Adsorption and Photocatalysis," *ENERGY & ENVIRONMENTAL MATERIALS* 5 (2022): 711–730, https://doi.org/10.1002/eem2.12229.

38. W. Lin, F. Lin, J. Lin, Z. Xiao, D. Yuan, and Y. Wang, "Efficient Photocatalytic CO_2 Reduction in Ellagic Acid–Based Covalent Organic Frameworks," *Journal of the American Chemical Society* 146 (2024): 16229–16236, https://doi.org/10.1021/jacs.4c04185.

39. R. Liu, Y. Chen, H. Yu, et al., "Linkage-Engineered Donor–Acceptor Covalent Organic Frameworks for Optimal Photosynthesis of Hydrogen Peroxide From Water and Air," *Nature Catalysis* 7 (2024): 195–206, https://doi.org/10.1038/s41929-023-01102-3.

40. G. Wu, F. Yu, H. Lei, S. Xiao, F. Song, and J. Qiu, "Sulfone Molecular Switch Enables Direct Two-Electron Uranium Photoreduction in Programmed Covalent Organic Frameworks," *Advanced Materials* (2025): 19608, https://doi.org/10.1002/adma.202519608.

41. P. Dong, J. Huang, S. Wu, et al., "Photogenerated Radical Amplified D-A-D Metal-Covalent Organic Frameworks for Highly Efficient Photodynamic Tumor Therapy," *Angewandte Chemie International Edition* 138 (2025): 20867.

42. X. Chi, Z. Zhang, M. Li, et al., "Vinylene-Linking of Polycyclic Aromatic Hydrocarbons to π-Extended Two-Dimensional Covalent Organic Framework Photocatalyst for H_2O_2 Synthesis," *Angewandte Chemie International Edition* 64 (2025): 202418895.

43. P. Huang, M. Yang, S. Zhang, et al., "Hydrogen-Localization Transfer Regulation in 3D COFs Enhances Photocatalytic Acetylene Semi-Hydrogenation to Ethylene," *Angewandte Chemie International Edition* 64 (2025): 202423091, https://doi.org/10.1002/anie.202423091.

44. S. Ma, Z. Li, Y. Hou, et al., "Fully Conjugated Benzobisoxazole-Bridged Covalent Organic Frameworks for Boosting Photocatalytic Hydrogen Evolution," *Angewandte Chemie International Edition* 64 (2025): 202501869.

45. M. Liu, J. Liu, J. Li, et al., "Blending Aryl Ketone in Covalent Organic Frameworks to Promote Photoinduced Electron Transfer," *Journal of the American Chemical Society* 145 (2023): 9198–9206, https://doi.org/10.1021/jacs.3c01273.

46. Z. Chen, J. Wang, M. Hao, et al., "Tuning Excited State Electronic Structure and Charge Transport in Covalent Organic Frameworks for Enhanced Photocatalytic Performance," *Nature Communications* 14 (2023): 1106, https://doi.org/10.1038/s41467-023-36710-x.

47. M. Peydayesh, E. Boschi, F. Donat, and R. Mezzenga, "Gold Recovery From E-Waste by Food-Waste Amyloid Aerogels," *Advanced Materials* 36 (2024): 2310642, https://doi.org/10.1002/adma.202310642.

48. S. Dutta, E. Lizundia, J. Goscianska, et al., "MOFs and COFs for Radionuclide and Nuclear-Waste Treatment," *Advanced Materials* 37 (2025): 18734, https://doi.org/10.1002/adma.202418734.

49. J. Zhao, Z. Qiao, Y. He, et al., "Anion-Regulated Ionic Covalent Organic Frameworks for Highly Selective Recovery of Gold From E-Waste," *Angewandte Chemie International Edition* 64 (2025): 202414366, https://doi.org/10.1002/anie.202414366.

50. L. Zhang, Q.-Q. Zheng, S.-J. Xiao, et al., "Covalent Organic Frameworks Constructed by Flexible Alkyl Amines for Efficient Gold Recovery From Leaching Solution of E-Waste," *Chemical Engineering Journal* 426 (2021): 131865, https://doi.org/10.1016/j.cej.2021.131865.

51. X. Qiao, L. Hao, H. Ren, et al., "Synergistic Effects of Nitrogen and Oxygen Active Sites in Covalent Organic Frameworks for Highly Efficient Gold Recovery," *Angewandte Chemie International Edition* 137 (2025): 202508162.

52. M. Liu, D. Jiang, Y. Fu, et al., "Modulating Skeletons of Covalent Organic Framework for High-Efficiency Gold Recovery," *Angewandte Chemie International Edition* 63 (2024): 202317015, https://doi.org/10.1002/anie.202317015.

53. M. Liu, H. Kong, S. Bi, et al., "Non-Interpenetrated 3D Covalent Organic Framework With Dia Topology for Au Ions Capture," *Advanced Functional Materials* 33 (2023): 2302637, https://doi.org/10.1002/adfm.202302637.

Supporting Information

Additional supporting information can be found online in the Supporting Information section.

Supporting File: adma72446-sup-0001-SuppMat.docx.